Experimental Quantification of Vent Mechanism Flow Parameters in 18650 Format Lithium Ion Batteries

Frank Austin Mier
Department of Mechanical Engineering,
New Mexico Institute of Mining and Technology,
Socorro, NM 87801
e-mail: frank.mier@student.nmt.edu

Michael J. Hargather
Department of Mechanical Engineering,
New Mexico Institute of Mining and Technology,
Socorro, NM 87801
e-mail: michael.hargather@nmt.edu

Summer R. Ferreira
Advanced Power Sources R&D,
Sandia National Laboratories,
Albuquerque, NM 87123

Lithium ion batteries have a well-documented tendency to fail energetically under various abuse conditions. These conditions frequently result in decomposition of the electrochemical components within the battery resulting in gas generation and increased internal pressure which can lead to an explosive case rupture. The 18650 format cell incorporates a vent mechanism located within a crimped cap to relieve pressure and mitigate the risk of case rupture. Cell venting, however, introduces additional safety concerns associated with the flow of flammable gases and liquid electrolyte into the environment. Experiments to quantify key parameters are performed to elucidate the external dynamics of battery venting. A first experiment measures the vent burst pressure. Burst vent caps are then tested with a second experimental fixture to measure vent opening area and discharge coefficient during choked-flow venting, which occurs during battery failure. Vent opening area and discharge coefficient are calculated from stagnation temperature, stagnation pressure, and static pressure measurements along with compressible-isentropic flow equations and conservation of mass. Commercially sourced vent caps are used with repeated tests run to quantify repeatability and variability. Validation experiments confirmed accuracy of opening area and discharge coefficient measurement. Further, trials conducted on vent caps from two sources demonstrate the potential for variation between manufacturers. [DOI: 10.1115/1.4042962]

1 Introduction

Lithium ion batteries have the ability to fail energetically when subjected to conditions outside of the intended usage environment. Battery failures are often associated with risks of flammability. Timelines of high profile battery failures show a persistent and ongoing need to mitigate risks [1]. By understanding the failure process, risks can be better assessed, thus leading to improved safety in all applications of lithium ion batteries.

Conditions which can lead to battery failures include overcharge, over-discharge, high temperature, low temperature, overcurrent, internal defects, mechanical loading (shock, crush, and penetration), and age [2]. Abuse conditions generally initiate a rise in temperature which drives exothermic reactions within the cell. If these reactions become self-sustaining, the battery is said to be in thermal runaway [3]. Experiments have shown that the onset of thermal runaway generally occurs below 125 °C and continues to much higher temperatures depending on cell type and abuse factors [4]. These conditions can become a safety concern when the failure is not able to be contained within the cell and a venting event occurs, or if thermal runaway propagates to adjacent cells. The primary driver behind cell venting is the generation of gases internal to the cell. Oxygen gas is generated at the cathode of common cell chemistries including lithium–cobalt–oxide (LCO), nickel–cobalt–aluminum (NCA), and nickel–manganese–cobalt (NMC) [5]. Reactions within the electrolyte can lead to generation of flammable gases including ethane, methane, and others which increase pressure within the cell [3,6]. The combination of oxygen and flammable gases creates a scenario where combustion is possible regardless of the atmospheric composition.

Abuse testing often includes evaluating the thermal runaway process, chemical composition of vented material, or flammability risk of a given cell. The 18650 format cell, defined by its 18 mm diameter and 65 mm length, is often used in laboratory scale calorimetry where the relations between state of charge (SOC), calorimeter pressure, peak temperature, and test duration are compared. In general, experiments have shown increased calorimeter pressures, peak temperature, and minimized test duration as SOC is increased [7]. Calorimetry experiments have been used to subject cells to extreme conditions with failure modes such as "jelly roll" ejection where the vent completely fails and the electrochemical components of the battery exit the case [8]. Cone calorimetry tests on LCO 18650 cells have been used for sampling of vented material throughout thermal abuse testing which showed increased concentrations of vented carbon monoxide and carbon dioxide for cells at higher initial SOC [9]. Imaging within cells during thermal abuse testing has been achieved by real time x-ray computed tomography scanning. When coupled with infrared imaging of the surface of an 18650 cell, internal failure was noted to correspond with a hot spot on the outside of the battery case [10]. High-speed imaging has been combined with thermal and chemical analysis to evaluate battery failures within a closely packed arrangement [11]. Schlieren imaging has been used to observe gas and liquid venting from lithium ion batteries under thermal abuse and overcharge [12]. While significant experimental research has been performed on the science of battery failures, methods to quantify the fluid dynamics of battery venting which occurs in some cell failure scenarios have not yet been fully developed.

Safety mechanisms are designed and fabricated into lithium ion batteries to mitigate the potential for catastrophic failures at the cell level as shown in Fig. 1. Current interrupt devices electrically disconnect the electrochemical components of a battery from external circuitry if conditions within the cell present high venting failure risk [13]. Cylindrical batteries usually have a current interrupt device which physically breaks an electrical connection when significant pressure is applied to a diaphragm which renders the battery permanently disconnected from external circuits [14].
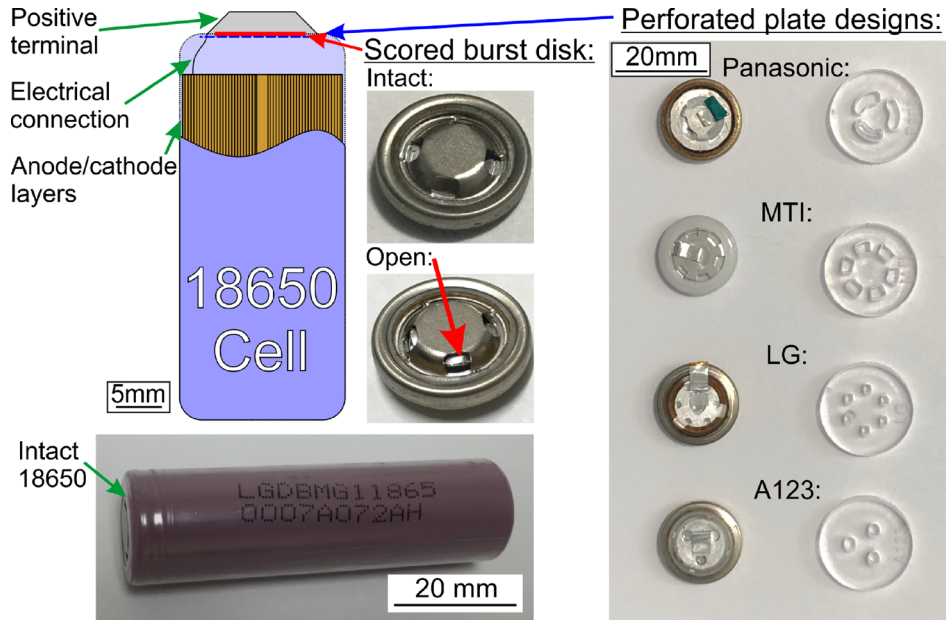
Fig. 1 A schematic representation of an 18650 format battery showing safety mechanisms and views of a vent cap with an intact and open burst disk. The bottom-left image shows an LG brand 18650 cell before disassembly. The internal surface of battery vent caps shows perforated plate designs from 18650 format cells made by LG, Panasonic, A123, and MTI. Mock orifice plates made to mimic the maximum possible opening area for measurement validation experiments.

Additional safety mechanisms include positive temperature coefficient elements which increase electrical resistance at elevated temperatures. The phenomena of separator shutdown can also act as a passive safety element to protect against high internal cell temperatures [15]. The final safety mechanism within most cylindrical batteries is a burst disk designed to open prior to case rupture.

While extensive work has described the relative risks of different cell chemistries and how broadly different batteries respond to abuse, a detailed analysis of how individual features in the construction of the ubiquitous 18650 format battery relate to battery failure characteristics has not yet been performed. Constraints have been applied when analyzing battery venting including a stated burst pressure of 3448 kPa [16]. This has been further applied to model the venting process from 18650 cells using isentropic flow equations and an initially choked flow [17]. However, expanding the level to which venting parameters are quantified will assist the evaluation of battery failures regardless of abuse condition or cell chemistry.

Experimental methods and test fixtures have been developed and applied here to characterize the venting process of 18650 format lithium ion batteries. Specifically, burst pressure, opening area, and discharge coefficient are quantified. These parameters affect the external fluid dynamics and duration of a venting failure which are directly related to safety risks including flammability. Vent caps, separated from live batteries, are tested to allow precise control of experiments with air rather than a volatile gas and liquid electrolyte spray.

2 Vent Cap Burst Experiment

2.1 Burst Measurement Fixture Design and Fabrication. A test fixture was constructed for direct pressurization of intact vent caps with compressed air. To achieve this, the holding mechanism shown in Fig. 2 was designed and fabricated. The vent cap is held securely between a high pressure fitting and a hollow lock set screw. Laser cut silicone gaskets on either side of the vent cap seal the fixture. Commercial off-the-shelf pipe fittings were used

to construct the vent cap holding fixture without needing complicated fabrication.

Air is supplied via a 11.5 mm inner diameter tube which is connected to the fixture with a stainless steel Swagelok® tube fitting. The air supply was directed through a ball valve to the main fixture body which was used to stop the flow of air after the vent opened. This main fixture body was constructed from pipe fittings which allow for a pressure measurement port. A straight-threaded section was used around the vent cap to allow for variability in thickness. Silicone gaskets sealed between the upstream compressed air and vent cap. A hollow lock set screw was used to compress the gaskets and vent cap, and the 12.7 mm hexagon used
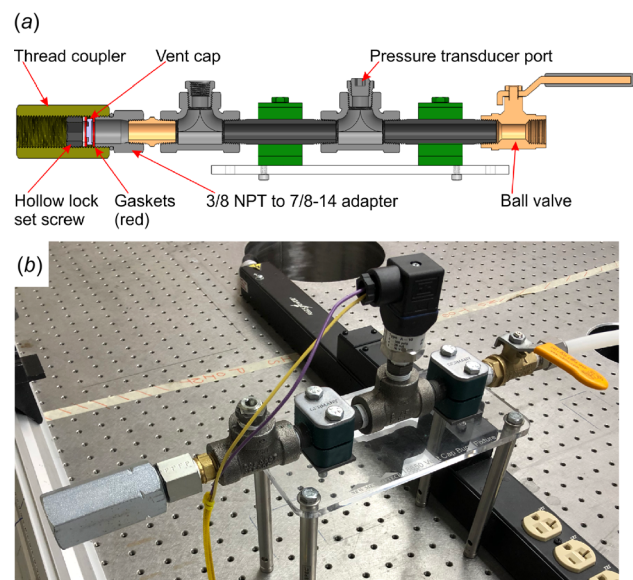
Fig. 2 The vent cap holding mechanism used for burst pressure tests is shown: (a) as an annotated cutaway schematic of the design and (b) as installed

for tightening the set screw allowed for an airflow channel once the vent cap bursts.

The vent cap holding fixture was mounted to an acrylic plate which is supported by four posts on an optical table. A length of high-pressure rated nylon tubing connects the vent cap holder to the compressed air supply which is regulated between 0 MPa and 3.45 MPa. The pressure regulator was operated manually by increasing the pressure to failure during testing. A dial type pressure gauge was used on the outlet of the regulator to confirm the reading from the pressure transducer installed on the vent cap holder. A compressed air cylinder was used as the high pressure gas source for vent testing. While there is little discussion in the literature of burst pressures for battery vents and no clearly standardized testing procedure for this parameter, the burst pressure test fixture designed here provided a simple and direct approach.

2.2 Procedure and Sample Data Analysis. Trials were begun by confirming a zero pressure reading and initiating data recording in LabVIEW by the test operator from a control room. The dial on the pressure control regulator was slowly and consistently turned manually by the operator in the test chamber to increase output pressure. A computer monitor allowed monitoring of a real-time pressure plot. The plot was monitored as pressure was increased to ensure that no erratic or rapid pressure changes occur, so the test could be considered to have been operated in a quasi-static manner. Pressure was increased manually until the vent cap opened. At this moment, the operator stopped adjusting the pressure regulator and immediately closed the ball valve to stop the flow of air. Figure 3 shows the pressure recorded during a single trial. The average time duration of a burst test was 25 s, and there was no trend between burst pressure and time duration. Dynamic gas effects and rate dependence of material properties are assumed to be insignificant in this experiment.

3 Choked Orifice Testing Apparatus

3.1 System Overview. Battery venting involves transient, pressure-driven, multiphase fluid flow through an orifice into the atmosphere. The multiphase flow is further complicated by ongoing decomposition reactions of the liquid electrolyte resulting in gas production, and ultimately difficult to quantify material properties. The intricate and unique geometry of the vent caps also adds to the complexity of opening area and discharge coefficient measurements.

The choked orifice testing apparatus (COTA) has been designed and fabricated to mimic the venting of gas through an 18650 size vent cap, but with simplifications made to allow for precise
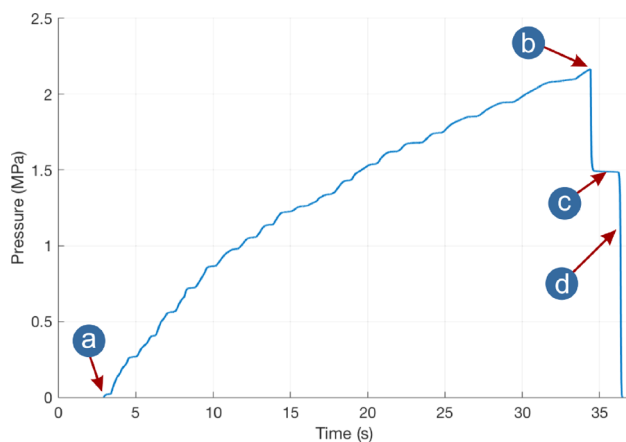
Fig. 3 Annotated pressure trace taken from an MTI vent cap test showing the: (*a*) beginning of pressurization, (*b*) vent burst, (*c*) flow momentarily choking, and (*d*) the ball valve being closed by the operator to stop airflow and finish the experiment

quantification of the flow. The test uses a large volume of dry air with well-known properties to allow for longer test times and better data acquisition. Removing the multiphase aspect of the flow removes the viscous effects and gas–liquid interaction which would limit flow rate and discharge coefficient. As such, the flow rates seen here will be an upper limit to the vent performance to be expected in live cell testing. The relative amounts gas and liquid vented from cells is a complicated function of cell chemistry, design, and abuse condition. Further, values of gas flow rate determined here describe relative performance between tests and vent designs, but vented decomposition products will have different ratios of specific heat (γ) based on cell chemistry.

Since the COTA has a pressure rating lower than the vent burst pressure, the vent caps used for testing with the COTA have all been previously tested on the aforementioned burst pressure measurement test fixture. The design of the vents is such that they will remain open after the initial burst test. This allows for retesting with the COTA to determine the opening area and discharge coefficient.

Figure 4 shows annotated images of the COTA and its individual components including the battery vent cap holder, an accumulator tank, pressure regulators, inlet and outlet valves, a compressed air cylinder, and instrumentation.

3.2 Nozzle Design of the Battery Vent Cap Holder. The battery vent cap holder within the COTA is designed to securely hold vent caps once removed from a battery and create an airtight seal with the upstream source of pressurized air. The vent cap holder can be seen installed in the test setup in Figs. 4(*a*) and 4(*b*). The hollow lock set screws and silicone gaskets from the burst pressure test fixture are also used in the COTA for sealing while allowing unobstructed gas flow. A short length of tubing connects the battery cap fixture to the outlet valve and accumulator tank.

The center of the battery vent cap holder is machined to a precisely known cross-sectional area. A small sensing orifice with a diameter of 1.4 mm has been drilled into this known area for measurement of static pressure throughout testing which is used in calculations to determine the opening area of each vent cap. The sensing orifice leads to a pressure transducer which is mounted directly into the body of the vent cap holder. The cross-sectional area at the sensing orifice of 40.0 mm^2 was designed to be larger than the maximum possible opening area of a battery vent cap, based on a survey of the perforated plates on the internal side of vent caps from cells of interest. Additionally, care has been taken to select all fittings with sufficiently large cross-sectional areas between the accumulator tank and vent cap, to ensure that the venting flow will choke at the vent cap rather than anywhere else within the system. Further details of the design of the COTA are available in Ref. [18].

The internal flow between the accumulator tank and vent cap can be represented as an isentropic, one-dimensional nozzle as shown in Fig. 4. This assumption is made because the flow is clearly within the compressible regime and the entire length of the accelerated flow is approximately eight diameters thus minimizing frictional losses. The cross section decreases as the flow is accelerated from the tank to the exit plane at the opening of the battery vent cap. Sudden changes are prevented by allowing tapered transitions between different sections of the holder. By designing the vent cap holder as a converging nozzle, with the vent opening at the exit plane, opening area can be calculated when the physical state of the air and geometry of the flow channel are known at another point upstream within the nozzle.

3.3 Measurements and Data Acquisition. Temperature and pressure are recorded and monitored simultaneously with a National Instruments (Austin, TX) cDAQ data acquisition system controlled by a LabVIEW program written for this specific test. Similar to the burst pressure measurement testing, a 12 V_{DC} power supply is used to power both 0 kPa–345 kPa pressure transducers.

The 4 mA–20 mA current output is converted to a voltage measurement within the range of the NI 9205 analog card by measuring the voltage drop over a nominally 470 Ω resistor. Temperature is measured directly by a NI 9212 card with internal cold junction compensation, and the thermocouple lines have been shielded to minimize signal noise caused by nearby equipment. Data acquisition rates for the temperature and pressure measurements are 100 Hz and 1 kHz, respectively.

Manufacturer calibrations are used for temperature and pressure measurements as all instrumentation was purchased new for these experiments. An additional exposed junction, K-type thermocouple probe is used to measure room temperature throughout testing and is confirmed against an Extech SD700 portable weather station. Wika brand A10 pressure transducers are provided with factory calibration results with 7 Pa precision, and linearity is confirmed. A linear fit to this calibration data is used to calculate gauge pressure from the transducer's output current. The resistance of the nominal 470 Ω resistors used to convert between current output and an analog voltage measurement are measured with a Fluke 115 multimeter to 0.1 Ω resolution. Additional analog dial pressure gauges are installed on the COTA for test operator confirmation that measurements are accurate during testing.

3.4 Venting Parameter Calculation Methodologies.

The opening area of the vent cap is inferred via the measured relationship between static and stagnation pressures during testing while the flow is choked. Within the test setup, three distinct locations are considered: stagnation within the tank (0), the known cross section in the vent cap holder (1), and the opening in the battery vent itself (e).

Making the assumptions that the flow within the system is isentropic and the air behaves as an ideal gas, the Mach number (M_1) of the flow through the vent cap holder can be calculated via the isentropic flow relation

$$\frac{P_0}{P_1} = \left(1 + \frac{\gamma - 1}{2} M_1^2\right)^{\frac{\gamma}{\gamma - 1}} \tag{1}$$

Here, γ is the ratio of constant pressure to constant volume specific heats for the air [19,20]. Once Mach number is determined at a known cross-sectional area, it can be used to calculate the area at which the flow is choked (A^*), which is the vent area

$$\frac{A_1}{A^*} = \frac{1}{M_1} \left(\frac{\frac{\gamma + 1}{2}}{1 + \frac{\gamma - 1}{2} M_1^2}\right)^{\frac{\gamma + 1}{2 - 2\gamma}} \tag{2}$$

By inspection of the experimental setup, the sonic location (A^*) is clearly the opening area (A_e).

In all tests, the stagnation pressure is initially enough to create a choked flow condition where the flow is sonic within the vent cap because $P_0 > 1.89 P_{atm}$ [19]. Once stagnation pressure drops significantly and the flow is unchoked, Eqs. (1) and (2) can still be used with the additional assumption that the flow exits the system through the vent cap with static pressure equal to atmospheric pressure.

The discharge coefficient describes the efficiency of mass flow through a given obstruction compared to the maximum possible mass flow rate. The need for this parameter arises as analytical calculations often ignore viscous losses and turbulence for simplicity, but these effects become significant when the flow is concentrated through a relatively small orifice or other obstruction. In general, relationships which are informed by experimental data accurately calculate discharge coefficient as a function of geometry and pressure, but these equations are specific to unique flow configurations [21]. Discharge coefficient varies between zero and one and can be simply defined as the ratio between actual ($\dot{m}_a$) and theoretical mass flow ($\dot{m}_t$) rates.

The theoretical mass flow rate through a choked orifice is calculated by assuming isentropic flow as

$$\dot{m}_t = \frac{P_0}{\sqrt{RT_0}} A^* \sqrt{\gamma} \left(1 + \frac{\gamma - 1}{2}\right)^{\frac{\gamma + 1}{2 - 2\gamma}} \tag{3}$$

Mass flow rate is approximated from conservation of mass for an Ideal Gas for the venting process

$$\dot{m}_a = -\frac{V}{R} \cdot \frac{d}{dt}\left(\frac{P_0}{T_0}\right) \tag{4}$$

This method allows for a simple approximation of the actual mass flow rate from the system with the known tank volume and gas constant along with the already measured stagnation temperature and pressure. Of note, the discharge coefficient measurements taken here describe the entire vent cap which itself has constrictions at the perforated plate and openings within the positive electrical terminal.

3.5 Testing Procedure and Example Dataset.

After the vent cap is installed within its holder, the accumulator tank is pressurized to 276 kPa which is monitored within LabVIEW. Data recording is stopped once stagnation pressure reaches 6.8 kPa. Figure 5 shows a sample dataset from a system calibration trial. Stagnation pressure is initially at 276 kPa and drops immediately
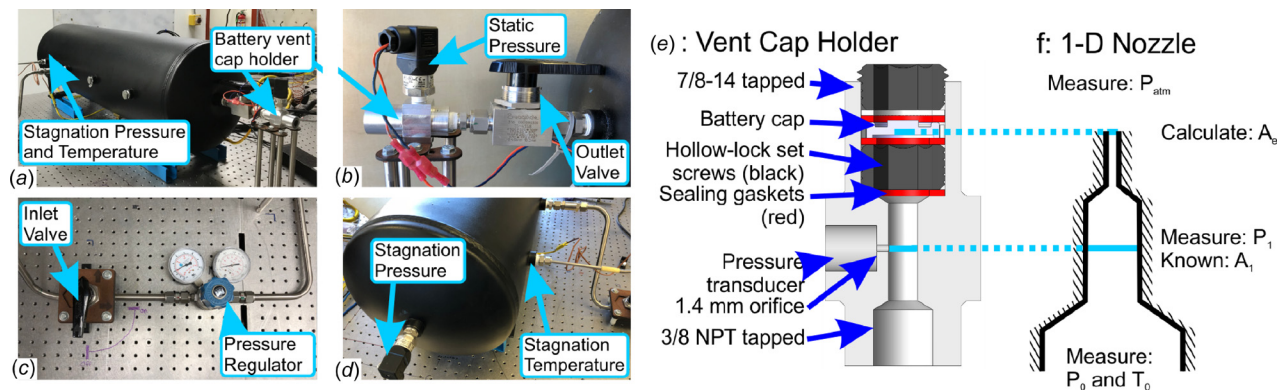
Fig. 4 Annotated views of the COTA showing the: (a) overall test setup, (b) battery vent cap holder with static pressure transducer and outlet valve, (c) the inlet valve and pressure regulator, and (d) the stagnation property measurement locations on the far end of the accumulator tank from the view in (a). (e) An annotated cutaway model of the vent cap holder compared to a (f) schematic representation of the vent cap holder as a one-dimensional nozzle with varying cross section. Horizontal blue lines show the relative locations of the vent cap and static pressure measurement between the model and schematic.

when the outlet valve is opened while static pressure jumps up to the appropriate value for the given opening area. The ratio of the absolute static pressure to stagnation pressure (P_1/P_0) is constant while stagnation pressure is above 76 kPa (gauge) as is expected because the flow is choked.
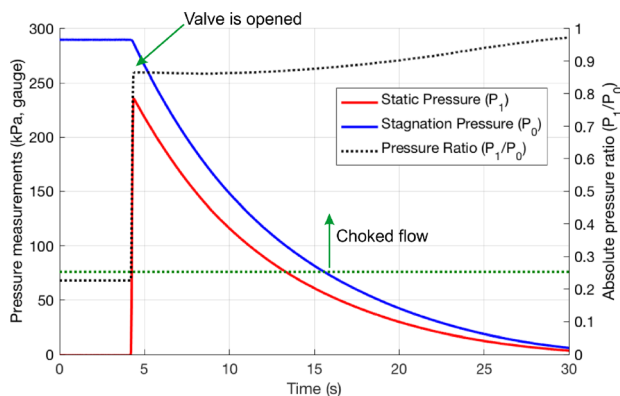
3.6 Experimental Validation With Known Orifices. A series of orifice plates were fabricated for validation of the opening area calculation methodology. These plates were installed and tested as direct substitutes for the battery vent cap in the COTA. Twenty circular orifices ranging in area from 3.16 mm^2 to 37.4 mm^2 were tested. Each circular validation orifice is sized to correspond with a number or letter gauge drill bit.

Four mock vent orifices seen in Fig. 1 were created representing the intricate geometry and maximum opening area of commercially available vent caps manufactured by LG, Panasonic, A123, and MTI cap. This was done by mimicking the cutouts in the perforated plate on the interior side of the vent cap. While the actual cross-sectional area of the vent opening is likely smaller than this, the perforated plate is a clear upper limit to the opening area.
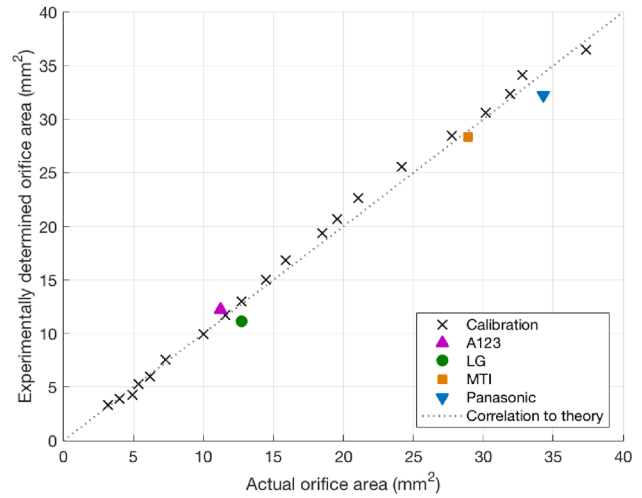
Individual trials with each of the circular orifices show strong agreement between physically measured and experimentally calculated opening areas throughout the range of possible vent cap opening areas. The results of this validation series are presented in Fig. 6 which demonstrates a clear correlation between actual and calculated opening areas. This validation series shows no significant skew or bias throughout the range of potentially measurable opening areas. The first third of circular orifices had an average 4.3% difference between calculated and actual area while the last third had an average 3.6% difference indicative of the increased difficulty of measuring opening area when the pressure ratio P_1/P_0 approaches unity. The orifices designed to mimic the battery vent caps show similar agreement.

Additional test orifices were fabricated to match some of the experiments by Kayser and Shambaugh who reported extensive experimental results including discharge coefficient in choked flow conditions [22]. Straight bore "S1" and "S2" orifices were turned from aluminum stock with interior diameters of 1.13 mm and 1.41 mm, respectively, and both orifices have a thickness of 3.17 mm. The drilled holes are left with sharp edges as done by Kayser and Shambaugh [22].

Discharge coefficient was calculated throughout the choked duration of the test and compared to the data reported by Kayser and Shambaugh [22]. Discharge coefficient is plotted against the stagnation pressure normalized by atmospheric pressure, and the datasets are compared in Fig. 7. This testing demonstrates that the discharge coefficient measurements with the COTA contain similar trends to previous experiments. Specifically, discharge coefficient is constant when P_0/P_{atm} is between 2.25 and 3.50 and discharge coefficient increases with opening area. The values


Fig. 6 Comparison between physically measured and calculated opening areas from the COTA validation series. Orifices with circular and more complex geometries can be measured accurately with this experiment and calculation methodology. Experimentally determined opening areas had an uncertainty smaller than the symbol size on the plot.

measured with the COTA are, on average, 7.0% higher than Kayser and Shambaugh's data for the S1 orifice and 14% higher for S2. The discharge coefficient values reported by Kayser and Shambaugh used a direct measurement of the actual flow rate through the orifices with two calibrated thermal mass flowmeters. As shown in Eq. (4), the actual flow rate in the discharge coefficient calculations presented here is simply an approximation tied to the Ideal Gas Law. The difference between the magnitude of the experimental discharge coefficient and the value from literature is attributed to the uncertainty within the mass flow rate calculations further discussed in Sec. 4.4.1.

4 Experimental Results and Data Analysis

4.1 Burst Pressure Measurements. A main test series of 50 commercially sourced vent caps from MTI and another set of four vents removed from live LG HE2 batteries were tested for burst pressure, opening area, and discharge coefficient. The size of the MTI test series allows for evaluation of the statistical distribution of vent cap burst and venting parameters. LG tests have not been exhaustively performed due to the complexities of the disassembly of live batteries.

Fig. 5 Example dataset from validation testing on the COTA with a mock MTI orifice
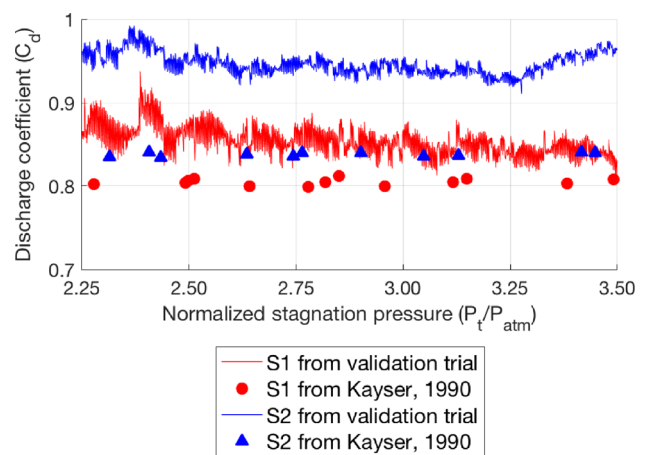
Fig. 7 Discharge coefficient versus normalized stagnation pressure for testing with S1 and S2 orifices

After performing the 50 MTI tests, statistical properties were calculated and a reported in Table 1. The dataset closely followed a normal distribution. Additionally, the minimum and maximum values for burst pressure are roughly the same distance from the mean.

The LG tests had burst pressure statistics listed in Table 1. This limited trial set has significantly lower burst pressures than the MTI caps. All LG burst pressures are lower than the minimum burst pressure from the MTI series.

4.2 Additional Observations From Vent Cap Burst Trials.

After some of the trials, the burst disk would become entirely detached within the vent cap. In all cases, the positive electrical terminal of the battery blocks the burst disk from being launched out of the test apparatus as a projectile. Specifically, 15 of the 50, or 30%, of the MTI vent caps showed complete disk detachment while no LG cell had a full detachment.

Once segregated into vent caps with burst disks remaining attached or becoming detached after testing, Fig. 8 shows two trends. The attached vent caps remained close to the normal distribution. While the detached burst disks had a similar mean burst pressure (2.177 MPa detached, 2.150 MPa attached). The trials with detached burst disks showed a skew biased toward higher burst pressures.

In testing both the MTI and the LG vent caps, an audible response from the vent cap was noticed at approximately 1 MPa. The sound was sufficiently loud to be heard while wearing hearing protection, and both test operators described it as a "tick" or a small "pop." A test was performed with an MTI vent cap where pressure was increased as normal, but when the audible response from the vent cap was heard, the pressure regulator setting was held constant and pressure was released manually. Upon removal from the test fixture, the electrical connection between the perforated plate and the burst disk was observed to be broken as indicated by two small holes near the foil tab. As such, the audible response from the vent caps during burst pressure testing is the instant when the current interrupt devices breaks and the battery would fail electrically as an open-loop.

As shown in Fig. 9, a Photron SA-X2 high speed digital camera imaged an MTI vent cap opening at a frame rate of 100 kHz, and second trial with a new vent cap was performed using high-speed schlieren imaging at 40 kHz. Testing showed that there was a single initial opening location which then spread circumferentially around nearly the entire scored burst disk. The complete opening of the vent cap was observed to occur before 90 μs. This opening pattern is similarly represented in the schlieren image set where venting is initially seen near the top of the vent cap (within the field of view) and eventually establishing the bottom jet as the entire cap opens. At later time scales when the burst disk has been completely ruptured, venting appears even across all openings in the positive terminal of the vent cap. Further details are available in Ref. [18].

4.3 Opening Area Measurements.

All 50 MTI vent caps used in the burst test series were retested with the COTA to measure opening area. Statistical properties of the opening area dataset from these tests are shown in Table 2. Prior to testing, the assumed maximum possible opening area of a vent cap would be the cross-sectional area of the perforated plate on the interior side of the burst disk, but comparison between this assumed maximum

of 24.98 mm^2 and the mean from the experimental dataset shows that the opening of the burst disk was consistently, significantly smaller.

The LG tests had opening area measurements listed in Table 2. All tests showed opening areas smaller than the maximum opening area as represented by openings of the perforated plate which were 12.71 mm^2.

In both the LG and MTI vent caps, the actual opening areas of the battery vents were much smaller than the openings in the perforated plate. The different manufacturers had vent caps with significantly different perforated plates, but the opening areas were fairly similar, even though manufacturers have different designs for the perforated plate within the battery. This would indicate that the feature which choked the flow was the opening around the circumference of the burst disk and the openings in the positive terminal which are very similar between cells.

4.4 Discharge Coefficient Calculations

4.4.1 Uncertainty Analysis. Uncertainty analysis has been performed to evaluate the precision of discharge coefficient calculations. To do this, uncertainties in the accumulator tank volume (ΔV), stagnation pressure (ΔP_0), stagnation temperature (ΔT_0), and opening area (ΔA^*) were propagated through calculation uncertainty of the actual and theoretical mass flow rates as $\Delta \dot{m}_a$ (Eq. (5)) and $\Delta \dot{m}_t$ (Eq. (6)), respectively. Values for the gas constant and ratio of specific heats for air are assumed to be precisely known scalars within each mass flow rate equation. Error propagation equations for mass flow rate follow the standard form for propagating error through equations with parameters that are multiplied and raised to numerical exponents [23]

$$\Delta \dot{m}_a = |\dot{m}_a| \sqrt{\left(\frac{\Delta V}{V}\right)^2 + \left(\frac{\Delta P_0}{P_0}\right)^2 + \left(\frac{\Delta T_0}{T_0}\right)^2} \qquad (5)$$

$$\Delta \dot{m}_t = |\dot{m}_t| \sqrt{\left(\frac{\Delta P_0}{P_0}\right)^2 + \left(\frac{0.5\Delta T_0}{T_0}\right)^2 + \left(\frac{\Delta A^*}{A^*}\right)^2} \qquad (6)$$

Since stagnation property values vary throughout testing, the uncertainty in both mass flow rates changes throughout the test. However, constant values for their uncertainties are used throughout. The uncertainty in the static and stagnation pressure measurements is chosen to be equal to the standard deviation of the noise band when measuring a constant pressure stored within the tank. This was calculated at 139 Pa when taking measurements at a rate of 1 kHz over the span of a few seconds. The uncertainty of the stagnation temperature measurement is the reported accuracy of the thermocouple by the manufacturer at 2 K [24].

Both accumulator tank volume and vent cap opening area have constant value and uncertainty during each individual test. The
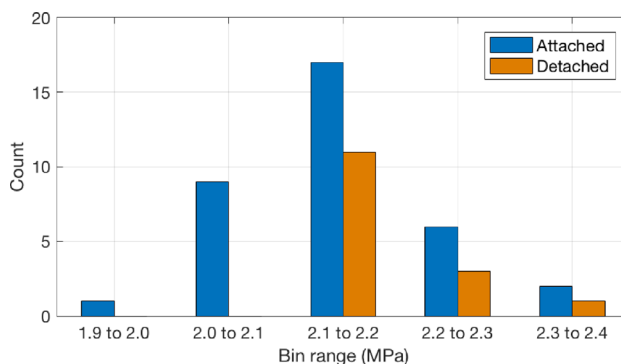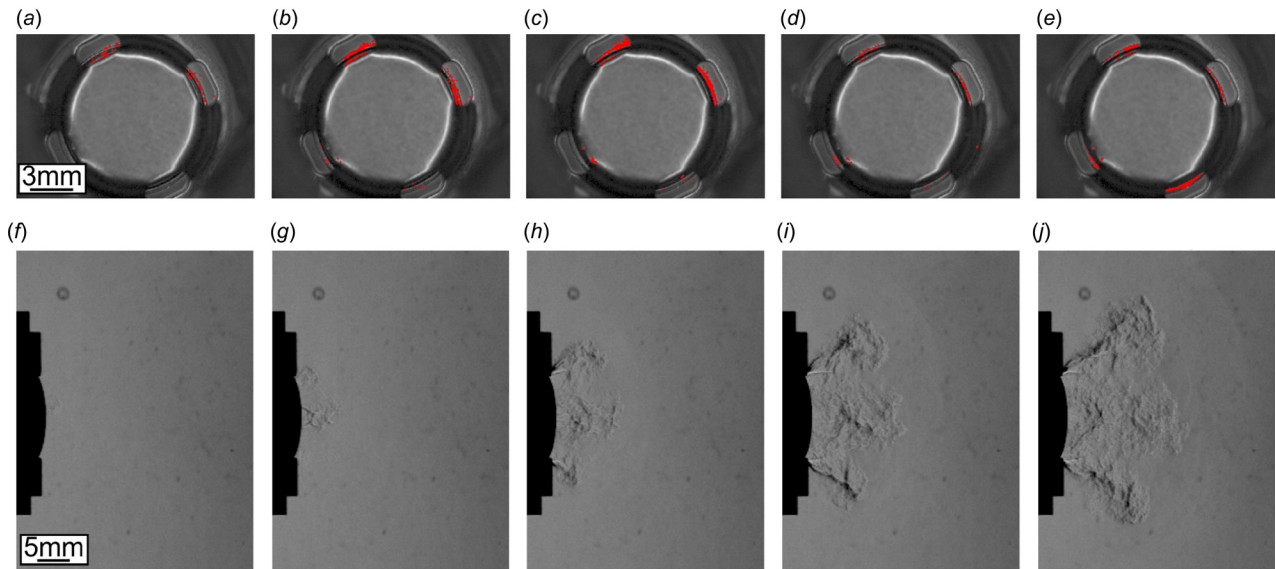
Table 1 Statistical properties of burst pressures

	MTI	LG
Mean	2.158 MPa	1.906 MPa
Minimum	1.971 MPa	1.829 MPa
Maximum	2.364 MPa	1.961 MPa
Standard deviation	0.081 MPa	0.060 MPa

Fig. 8 Histogram of MTI burst pressures from vent caps with attached and detached disks

Fig. 9 (*a*)–(*e*) High-speed images of burst disk opening (highlighted in red) around the disk circumference compared to (*f*)–(*j*) similarly sequenced high-speed schlieren images showing initially uneven venting: (*a*) $t = 0\,\mu$s, (*b*) $t = 20\,\mu$s, (*c*) $t = 40\,\mu$s, (*d*) $t = 60\,\mu$s, (*e*) $t = 80\,\mu$s, (*f*) $t = 0\,\mu$s, (*g*) $t = 20.8\,\mu$s, (*h*) $t = 41.7\,\mu$s, (*i*) $t = 62.5\,\mu$s, and (*j*) $t = 83.3\,\mu$s

accumulator tank volume of 74.3 L was measured by filling the tank completely with water and then measuring the volume of the water with an uncertainty of 0.4 L.

To calculate the uncertainty of an opening area measurement, static and stagnation pressure uncertainties were propagated through Eqs. (1) and (2). Since these equations are algebraically complicated, uncertainty was propagated using the general form of a parameter being a function of multiple other parameters

$$\Delta M_1 = \sqrt{\left(\frac{\partial M_1}{\partial P_0}\Delta P_0\right)^2 + \left(\frac{\partial M_1}{\partial P_1}\Delta P_1\right)^2} \tag{7}$$

$$\Delta A^* = \sqrt{\left(\frac{\partial A^*}{\partial M_1}\Delta M\right)^2 + \left(\frac{\partial A^*}{\partial A_1}\Delta A_1\right)^2} \tag{8}$$

Equations (7) and (8) describe how Mach number uncertainty (ΔM_1) was first calculated from static and stagnation pressure and then propagated with uncertainty in the known cross-sectional area (ΔA_1) to calculate uncertainty in choked opening area (ΔA^*). Uncertainty in the known cross-sectional area was calculated to be 0.6 mm^2. This is equivalent to diameter variation of 0.03 mm as this was the degree of measurement on the digital calipers used to confirm the diameter of the drilled cross section.

4.4.2 Determination of Stagnation Pressure Range for Valid Discharge Coefficient Measurement. Discharge coefficient values are reported as a function of normalized stagnation pressure in Fig. 10. The time scale of experiments is determined by the size of the accumulator tank, which is continually decreasing in stagnation pressure as the test occurs. Because the stagnation pressure decreases monotonically, the pressure axis is proportional to time if read in a right to left manner. Since the actual mass flow rate

can never be greater than the actual mass flow, discharge coefficient values greater than one are not physically possible. The
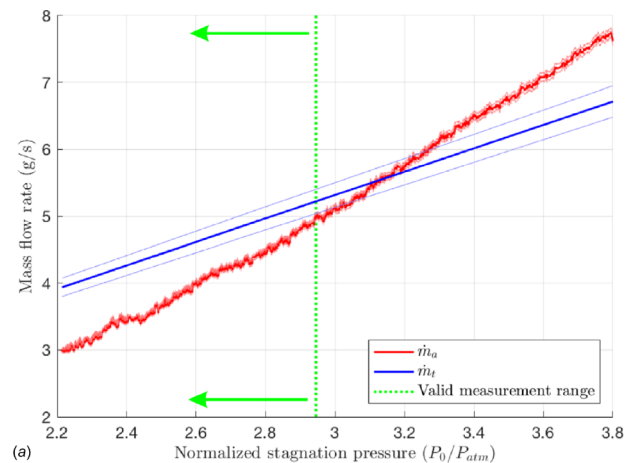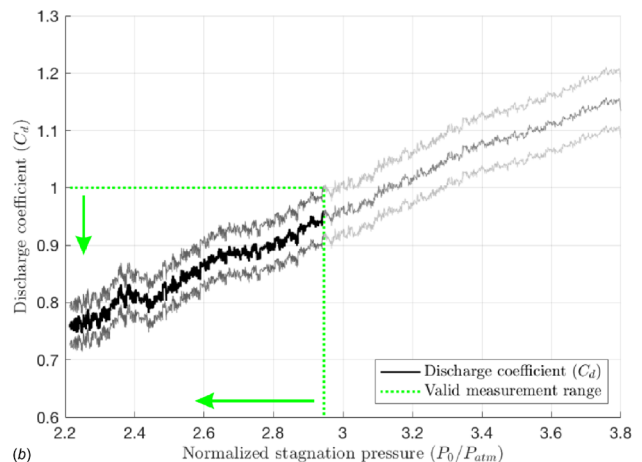
Fig. 10 (*a*) Bounded actual and theoretical mass flow rates for MTI Trial 22 showing the valid measurement range and (*b*) the subsequent discharge coefficient calculation plotted with upper and lower bounds

Table 2 Statistical properties of opening area measurements

	MTI	LG
Mean	8.967 mm^2	7.025 mm^2
Minimum	7.845 mm^2	6.111 mm^2
Maximum	9.773 mm^2	7.887 mm^2
Standard deviation	0.379 mm^2	0.769 mm^2

discharge coefficients are calculated to be greater than 1 at the beginning of the tests, which is assumed to be due to pressure and temperature measurement errors at the beginning of tests associated with time response and hysteresis in these highly transient measurements. As shown in Fig. 5, pressure measurements decrease more quickly at the beginning of each trial.

To define the region where the calculated discharge coefficient values are valid, the range of stagnation pressure values has been limited to where the largest possible actual flow rate is equal to or less than the minimum possible theoretical flow rate, accounting for the calculated uncertainties of both parameters. Expressed mathematically, the calculations are deemed valid when
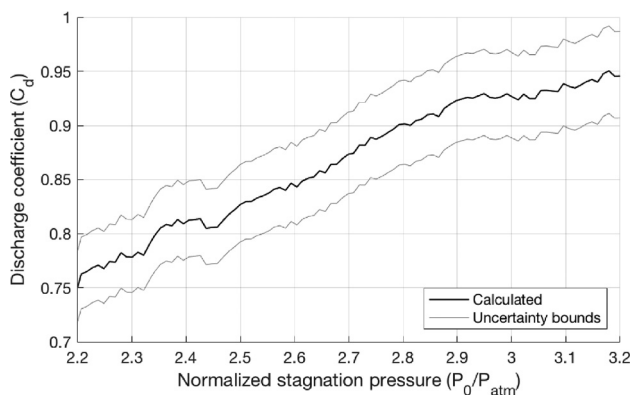
$$\dot{m}_t - \Delta\dot{m}_t \geq \dot{m}_a + \Delta\dot{m}_a \tag{9}$$

Graphically, the valid measurement range for a representative MTI cap was calculated to be left of the dashed line in Fig. 10(a) where the bottom of the theoretical mass flow rate uncertainty band met the top of the actual mass flow rate uncertainty band.

Additionally, the uncertainties in mass flow rate which led to minimum and maximum possible flow rates can be used to define upper and lower bounds for discharge coefficient. Figure 10(b) shows how calculated discharge coefficient values from a complete test dataset for a representative MTI trial were restricted to a valid measurement range. If measurement errors were reduced and the valid measurement range expanded, it is expected that the discharge coefficient approaches unity at higher stagnation pressures. At lower stagnation pressures, discharge coefficient is expected to decrease, but the mostly linear trend seen within the measurement range here would likely not be sustained.

4.4.3 Relationship Between Discharge Coefficient and Normalized Stagnation Pressure. To evaluate how discharge coefficient is related to stagnation pressure for the entire MTI testing series, the valid measurement range for each of the 50 trials was combined into a single dataset. The data were smoothed by calculating the mean discharge coefficient from raw data points within 100 equal sized pressure windows. This is shown in Fig. 11.

4.4.4 Statistical Distribution. For statistical evaluation of the discharge coefficient distribution, a constant normalized stagnation pressure of 2.6 was chosen for comparison between individual tests. This value was in the middle the measurement range of all MTI vent cap datasets. The mean discharge coefficient at this normalized stagnation pressure was 0.850 for the MTI vent caps, and statistical data are listed in Table 3. The uncertainty in the discharge coefficient at this value, being the difference $C_{d,\max} - C_{d,\min}$, is 0.073 ($\pm$0.037) at this normalized stagnation pressure. Table 3 lists the calculated statistical properties. The

data collected indicate that the discharge coefficient values were normally distributed.

Discharge coefficient for the LG vent caps was also calculated at a normalized stagnation pressure. Statistical properties are shown in Table 3. These values for discharge coefficient were consistently lower than the MTI vent caps.

4.5 Combined Burst Pressure, Opening Area, and Discharge Coefficient Results. As each vent cap was labeled and tracked throughout data analysis, vent mechanism parameters can thus be compared with each other between burst pressure measurement and COTA testing. Comparison between burst pressure, opening area, and discharge coefficients for the MTI vent cap test series shows slight or no correlation between these properties. Opening area and burst pressure did not appear to show a strong correlation.

In Figs. 12(a) and 12(b), discharge coefficients recorded at a normalized stagnation pressure of 2.6 showed slightly decreasing trends with increasing opening area and discharge coefficient, respectively. The trends are highlighted by the plotted linear regressions. While increases in opening area generally correlate to increased discharge coefficient, as seen in the circular orifice validation testing, more complicated orifices generally have smaller discharge coefficients. This is due to the fact that these geometries are more dissimilar to the quasi one-dimensional isentropic flow scenario used as the theoretical mass flow rate. Thus, the trend in Fig. 12(a) can be interpreted as showing that vent caps with larger opening areas tended to have less ideal flow conditions which had a greater effect on the discharge coefficient than the increase in opening area. However, while discharge coefficient may be decreased at larger opening areas, this simply states that the efficiency of the fluid flow is further from ideal. Actual mass flow rate can be solved from the definition of discharge coefficient and Eq. (3) parametrically assuming stagnation pressures and discharge coefficients are known.

Actual mass flow rate at a normalized stagnation pressure of 2.6 was plotted versus opening area in Fig. 13, and shows that the mass flow rate still increases proportionally to opening area. The effect of decreased discharge coefficient values at higher opening areas is negligible in the mass flow rate as a whole.

4.6 Simple Model of Battery Venting Parameters. From the measurements of burst pressure, opening area, and discharge coefficient, a simple model can be evaluated to begin description of the fluid dynamics of battery venting. The equations in Sec. 3.4 can be rewritten to attain the differential equation

$$\frac{dP_0}{dt} = -C_d \cdot \frac{P_0\sqrt{RT_0}}{V_0} A^* \sqrt{\gamma} \left(1 + \frac{\gamma-1}{2}\right)^{\frac{\gamma+1}{2-2\gamma}} \tag{10}$$

The initial condition is $P_0(t=0) = P_{\text{burst}}$. This equation is valid under choked flow conditions only. Solving this equation would be trivial under a constant discharge coefficient, but this parameter was demonstrated to vary with stagnation pressure in Fig. 11. As such, the equation was solved numerically with a fourth-order Runge–Kutta differential equation solver within MATLAB. The mean discharge coefficient profile versus pressure is approximated as a constant value of $C_d = 0.75$ below a normalized stagnation

Fig. 11 Binned and averaged values for discharge coefficient calculations from all 50 MTI vent cap tests showing the distribution of potential discharge coefficient values within the valid stagnation pressure range

Table 3 Statistical properties of discharge coefficients at $P_0/P_{\text{atm}} = 2.6$

	MTI	LG
Mean	0.850	0.814
Minimum	0.788	0.801
Maximum	0.903	0.832
Standard deviation	0.024	0.014
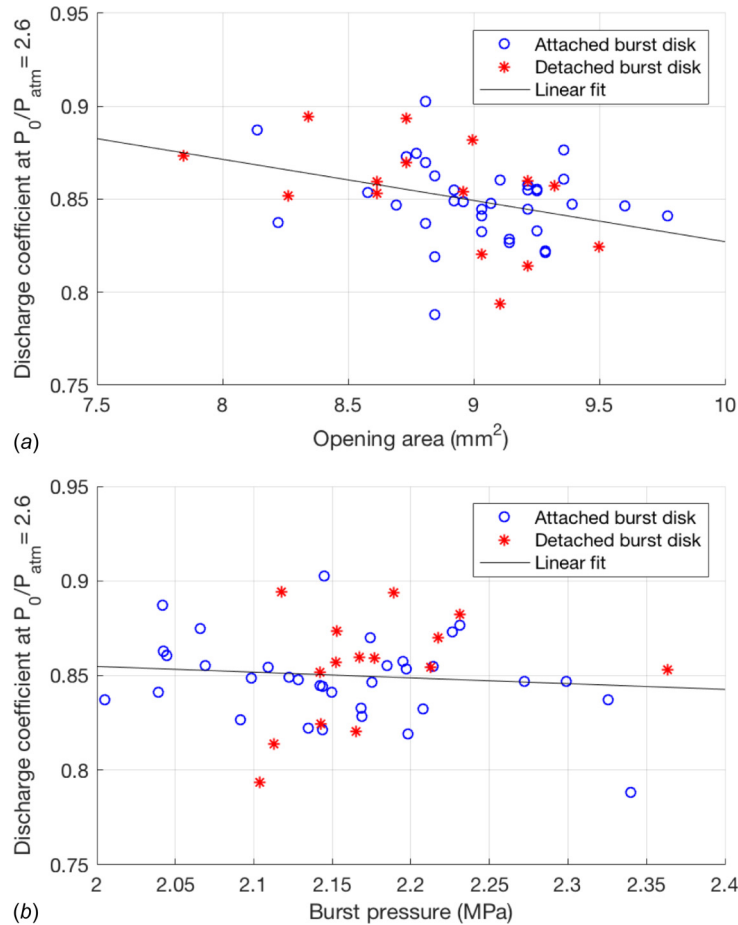
Fig. 12 Comparing discharge coefficient to: (*a*) opening area and (*b*) burst pressure from testing series of 50 MTI vent caps

pressure of $P_0/P_{atm} = 2.2$ and $C_d = 0.95$ above $P_0/P_{atm} = 3.2$ with a linearly varying section in the middle. The volume of the pressure reservoir within the battery was $1.52\,cm^3$ [25]. Last, venting calculations are made with $\gamma = 1.4$ representing air and a constant stagnation temperature of 293 K. Figure 14 shows the results of this model as battery stagnation pressure and the corresponding mass flow rate versus time under various scenarios where individual vent parameters are varied by two standard deviations as reported in Tables 1–3.
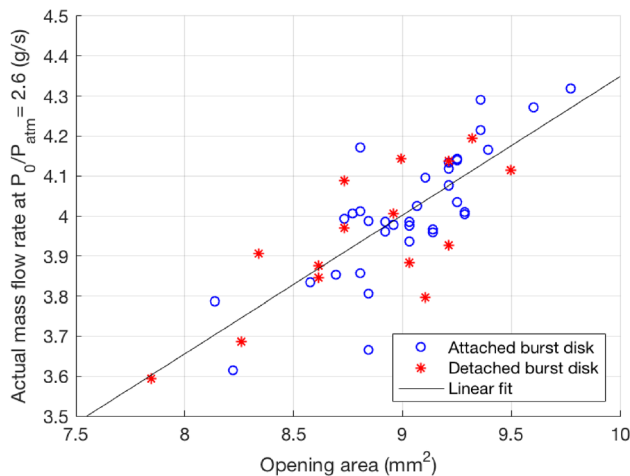

Fig. 13 Actual mass flow rate versus opening area for testing series of 50 MTI vent caps

Variation of individual parameters shows significant variation in battery pressure and flow rate throughout the venting process. Initially, burst pressure dominates the variation in battery pressure while burst pressure and opening area show similar importance to mass flow rate. In later time, as the flow approaches being unchoked, discharge coefficient variation becomes significant while the effects of different burst pressure decrease. Additionally, when using parameters presented in the recent modeling work of Coman et al. [17] for burst pressure (3.448 MPa) and opening area ($12.4\,mm^2$) along with a discharge coefficient of unity for isentropic flow, there is a significant discrepancy in pressure and mass flow rate within the first millisecond of venting when compared the scenarios based on measurements taken here. Burst pressure and opening area differences create the overwhelming majority of this discrepancy. While more complicated modeling is certainly possible, this approach demonstrates the basic effects of the parameters measured in this study and their importance within the body of literature. The calculated parameters here provide a boundary condition for the flow as time progresses beyond venting onset.

5 Conclusions

Experimental methods of measuring burst pressure, opening area, and discharge coefficient were developed for use on 18650 format lithium ion battery vents. The approach presented here allows quantification of discharge coefficient at relatively high flow rates without an in-line flow meter. The two test series conducted demonstrate that the vent parameters follow a normal distribution and can vary between manufacturers.

The mean burst pressure values of 2.158 MPa and 1.906 MPa for the MTI and LG cells, respectively, are significantly lower
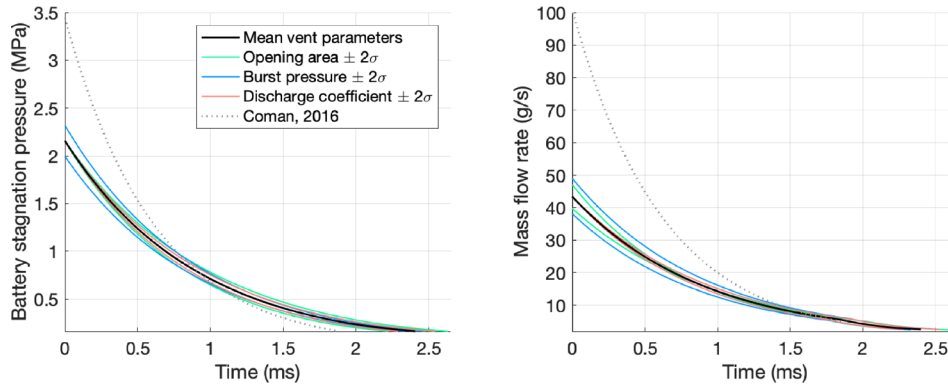
Fig. 14 Model predictions for pressure and mass flow rate versus time for gas venting from an 18650 cell

than the 3.448 MPa mentioned in the literature [16]. This indicates that venting occurs earlier than expected which may provide additional safety considerations. Venting gas flow chokes in the region of the vent cap around the circumference of the burst disk which is limited by the openings in the positive terminal. This opening has similar geometry between manufacturers, and average MTI and LG opening areas were accordingly comparable. While opening areas between different manufacturers are unrelated to perforated plate geometry, these differences in internal flow paths can manifest as different discharge coefficient values. On a vent-by-vent basis, discharge coefficient decreases with both increased opening area and burst pressure. However, actual mass flow rate still increased linearly with opening area. As such, the observed variability in opening area is the dominant parameter in venting flow rate differences between cells.

High-speed imaging showed a tendency of the burst disks to open from one single point with the opening progressing in both directions around the scored circle. This opening tendency can help describe the asymmetric venting seen initially in previous high speed schlieren imaging of battery failures [12].

Measurement of burst pressure, opening area, and discharge coefficient is an advancement in the understanding of battery failures and allows the external fluid dynamics of 18650 format lithium ion battery failures to be accurately characterized in analytical and computational models. These three parameters provide the necessary initial and boundary conditions to the flow which provides a more clear scientific understanding in all studies pertaining to venting failures of batteries and, broadly, any form of transient venting from a finite volume pressure reservoir. The simplified model of battery pressure as a function of time after venting onset presented here serves to highlight the importance of each individual parameter's effect on transient venting. These data may be applied to past research where battery venting under thermal runaway was modeled but the values of these vent parameters were estimated by necessity [17]. Regardless of the specific abuse conditions which lead to a venting failure, the additional ability to describe how venting will occur within its surroundings will assist in the assessment of battery related hazards.

Nomenclature

$A* =$ sonic cross-sectional area
$A_e =$ opening area
$A_1 =$ area at known cross section
$C_d =$ discharge coefficient
$\dot{m} =$ mass flow rate
$M_1 =$ Mach number at known cross section
$\dot{m}_a =$ actual mass flow rate
$\dot{m}_t =$ theoretical mass flow rate
$P_{atm} =$ atmospheric pressure
$P_0 =$ stagnation pressure (absolute)
$P_1 =$ pressure at known cross section (absolute)
$R =$ specific gas constant
$T_0 =$ stagnation temperature
$V =$ accumulator tank volume
$\Delta A* =$ uncertainty in $A*$
$\Delta M_1 =$ uncertainty in M_1
$\Delta \dot{m}_a =$ uncertainty in $\dot{m}_a$
$\Delta \dot{m}_t =$ uncertainty in $\dot{m}_t$
$\Delta P_0 =$ uncertainty in P_0
$\Delta P_1 =$ uncertainty in P_1
$\Delta T_0 =$ uncertainty in T_0
$\Delta V =$ uncertainty in V
$\gamma =$ ratio of specific heats

References

[1] Abada, S., Marlair, G., Lecocq, A., Petit, M., Sauvant-Moynot, M., and Huet, F., 2016, "Safety Focused Modeling of Lithium-Ion Batteries: A Review," J. Power Sources, **306**, pp. 178–192.
[2] Weicker, P., 2014, *A Systems Approach to Lithium-Ion Battery Management*, Artech House, Boston, MA.
[3] Wang, Q., Ping, P., Zhao, X., Chu, G., Sun, J., and Chen, C., 2012, "Thermal Runaway Caused Fire and Explosion of Lithium Ion Battery," J. Power Sources, **208**, pp. 210–224.
[4] Roth, E. P., Crafts, C. C., Doughty, D. H., and McBreen, J., 2004, "Advanced Technology Development Program for Lithium-Ion Batteries: Thermal Abuse Performance of 18650 Li-Ion Cells," Technical Report, Sandia National Laboratories, Albuquerque, NM, Report No. SAND2004-0584.
[5] Zhang, S. S., 2014, "Insight Into the Gassing Problem of li-Ion Battery," Front. Energy Res., **2**, pp. 1–4.
[6] Lamb, J., Orendorff, C. J., Roth, E. P., and Langendorf, J., 2015, "Studies on the Thermal Breakdown of Common Li-Ion Battery Electrolyte Components," J. Electrochem. Soc., **162**(10), pp. A2131–A2135.
[7] Chen, W. C., Li, J. D., Shu, C. M., and Wang, Y. W., 2015, "Effects of Thermal Hazard on 18650 Lithium-Ion Battery Under Different States of Charge," J. Therm. Anal. Calorim., **121**(1), pp. 525–531.
[8] Lyon, R. E., and Walters, R. N., 2016, "Energetics of Lithium Ion Battery Failure," J. Hazard. Mater., **318**, pp. 164–172.

[9] Fu, Y., Lu, S., Li, K., Liu, C., Cheng, X., and Zhang, H., 2015, "An Experimental Study on Burning Behaviors of 18650 Lithium Ion Batteries Using a Cone Calorimeter," J. Power Sources, **273**, pp. 216–222.

[10] Finegan, D. P., Scheel, M., Robinson, J. B., Tjaden, B., Hunt, I., Mason, T. J., Millichamp, J., Di Michiel, M., Offer, G. J., Hinds, G., Brett, D. J. L., and Shearing, P. R., 2015, "In-Operando High-Speed Tomography of Lithium-Ion Batteries During Thermal Runaway," Nat. Commun., **6**, p. 6924.

[11] Spinner, N. S., Field, C. R., Hammond, M. H., Williams, B. A., Myers, K. M., Lubrano, A. L., Rose-Pehrsson, S. L., and Tuttle, S. G., 2015, "Physical and Chemical Analysis of Lithium-Ion Battery Cell-to-Cell Failure Events Inside Custom Fire Chamber," J. Power Sources, **279**, pp. 713–721.

[12] Mier, F. A., Morales, R., Coultas-McKenney, C. A., Hargather, M. J., and Ostanek, J., 2017, "Overcharge and Thermal Destructive Testing of Lithium Metal Oxide and Lithium Metal Phosphate Batteries Incorporating Optical Diagnostics," J. Energy Storage, **13**, pp. 378–386.

[13] Jeevarajan, J., and Manzo, M., 2009, "Engineering and Safety Center Technical Bulletin," National Aeronautics and Space Administration, Hampton, VA, Report No. 09-02.

[14] Mikolajczak, C., Kahn, M., White, K., and Long, R. T., 2011, *Lithium-Ion Batteries Hazard and Use Assessment*, Springer, New York.

[15] Balakrishnan, P. G., Ramesh, R., and Prem Kumar, T., 2006, "Safety Mechanisms in Lithium-Ion Batteries," J. Power Sources, **155**(2), pp. 401–414.

[16] Buchmann, I., 2001, *Batteries in a Portable World a Handbook on Rechargeable Batteries for Non-Engineers*, Cadex Electronics, Richmond, BC, Canada.

[17] Coman, P. T., Rayman, S., and White, R. E., 2016, "A Lumped Model of Venting During Thermal Runaway in a Cylindrical Lithium Cobalt Oxide Lithium-Ion Cell," J. Power Sources, **307**, pp. 56–62.

[18] Mier, F. A., 2018, "Measurement of 18650 Format Lithium Richmond, BC V6W 1J6, Canada Ion Battery Vent Mechanism Flow Parameters," Master's thesis, New Mexico Institute of Mining and Technology, Socorro, NM.

[19] John, J. E., and Keith, T. G., 2006, *Gas Dynamics*, 3rd ed., Pearson Prentice Hall, Upper Saddle River, NJ.

[20] Cengel, Y. A., and Cimbala, J. M., 2010, *Fluid Mechanics Fundamentals and Applications*, 2nd ed., McGraw-Hill, New York.

[21] Czetany, L., and Lang, P., 2018, "Discharge Coefficients for Circular Side Outlets," ASME J. Fluids Eng., **140**(7), p. 071205.

[22] Kayser, J. C., and Shambaugh, R. L., 1991, "Discharge Coefficients for Compressible Flow Through Small-Diameter Orifices and Convergent Nozzles," Chem. Eng. Sci., **46**(7), pp. 1697–1711.

[23] Taylor, J. R., 1997, *An Introduction to Error Analysis*, University Science Books, New York.

[24] Omega, 2018, "Wire Color Codes and Limits of Error," L78 Datasheet, accessed Mar. 6, 2019, www.omega.com/techref/colorcodes.html

[25] Golubkov, A. W., Fuchs, D., Wagner, J., Wiltsche, H., Stangl, C., Fauler, G., Voitic, G., Thaler, A., and Hacker, V., 2014, "Thermal-Runaway Experiments on Consumer Li-Ion Batteries With Metal-Oxide and Olivin-Type Cathodes," RSC Adv., **4**(7), pp. 3633–3642.